A comparative study of far-field tsunami amplitudes and ocean-wide propagation properties: insight from major trans-Pacific tsunamis of 2010–2015

Mohammad Heidarzadeh,[1] Kenji Satake,[2] Tomohiro Takagawa,[3] Alexander Rabinovich[4,5] and Satoshi Kusumoto[2]

[1]*Department of Civil & Environmental Engineering, Brunel University London, Uxbridge* UB8 3PH, *UK. E-mail:* mohammad.heidarzadeh@brunel.ac.uk
[2]*Earthquake Research Institute, The University of Tokyo, Tokyo* 113-0032, *Japan*
[3]*Port and Airport Research Institute, Yokosuka* 239–0826, *Japan*
[4]*Institute of Ocean Sciences, Sidney, British Columbia,* V8L 4B2, *Canada*
[5]*Shirshov Institute of Oceanology, Russian Academy of Sciences, Moscow* 117997, *Russia*

SUMMARY

We studied ocean-wide propagation properties of four recent trans-Pacific tsunamis based on deep-ocean measurements across the Pacific Ocean. First, we analysed and simulated the 2015 September 16 tsunami generated by the Illapel (Chile) earthquake (M_w 8.4) and compared its ocean-wide propagation with those of three other events: the 2014 Iquique (M_w 8.2), 2010 Maule (M_w 8.8) and 2011 Tohoku (M_w 9.0). The Illapel and Maule tsunami sources are located close to each other and we reconstructed the source spectrum of the larger (i.e. Maule) tsunami by applying spectral deconvolution using the smaller (i.e. Illapel) tsunami as the empirical Green's function. The initial negative phase was found for all four events with durations of 8–29 (Iquique), 20–35 (Illapel), 22–70 (Maule) and 40–79 (Tohoku) min, with the maximum amplitudes of 0.11–0.26, 0.4–0.7, 0.5–2.9 and 1.9–2.5 cm, and the amplitude ratios to the first elevation phases of 20–40 per cent, 22–41 per cent, 29–61 per cent and 12–67 per cent, respectively. Unlike other studies, our results revealed that the duration (D_{ini}) and amplitude (A_{ini}) of the initial negative phase are directly proportional to the earthquake magnitude (M_w) with equations: $M_w = 6.129 + 1.629 \log(D_{ini})$ and $M_w = 8.676 + 0.706 \log(A_{ini})$. No relationships were observed between these parameters (i.e. D_{ini} and A_{ini}) and distance from the source. The amplitudes of far-field DART waves do not vary with distance or strike angle, and depend only on the M_w. The average far-field deep-ocean amplitudes (A_{tsu}) for the Iquique, Illapel, Maule and Tohoku tsunamis were 0.9, 1.7, 6.0 and 15.0 cm, respectively, yielding the equation: $M_w = 8.245 + 0.665 \log(A_{tsu})$.

Key words: Tsunamis; Pacific Ocean; Time-series analysis; Wavelet transform; Tsunami warning; Subduction zone processes.

1 INTRODUCTION

Although coastal observations of tsunamis by tide gauge stations started around 165 yr ago (Rabinovich & Eble 2015), deep-ocean observations of tsunamis are relatively new. Before the 2000s, only a few deep-ocean tsunami records were obtained in various parts of the Pacific Ocean (e.g. Filloux 1982; González *et al.* 1991; Okada 1995). These measurements were mostly based on short-term instrument campaigns which covered a limited area. The DART (Deep-ocean Assessment and Reporting of Tsunamis) project, started in the early 2000s, provided permanent real-time deep-ocean tsunami measurements through bottom pressure gauges from across the Pa-

cific Ocean (Synolakis & Bernard 2006; Mofjeld 2009). The number of DARTs was increased from seven in 2004 installed offshore of Alaska, the USA West Coast and Chile to ∼60 deployed in major seismic regions of the world oceans (Rabinovich & Eblé 2015).

Trans-Pacific tsunamis recorded on the DART network provide valuable information on tsunami behaviour in the open ocean. The most recent event of this type was the 2015 September 16 Illapel tsunami produced by an M_w 8.4 earthquake (Fig. 1). Other recent major tsunamigenic earthquakes in the Chilean subduction zone are the 2010 Maule (M_w 8.8) and the 2014 Iquique (M_w 8.2) earthquakes. The strongest event in the Pacific Ocean since 1964 was the 2011 Tohoku (Japan) earthquake (M_w 9.0) that generated a devas-
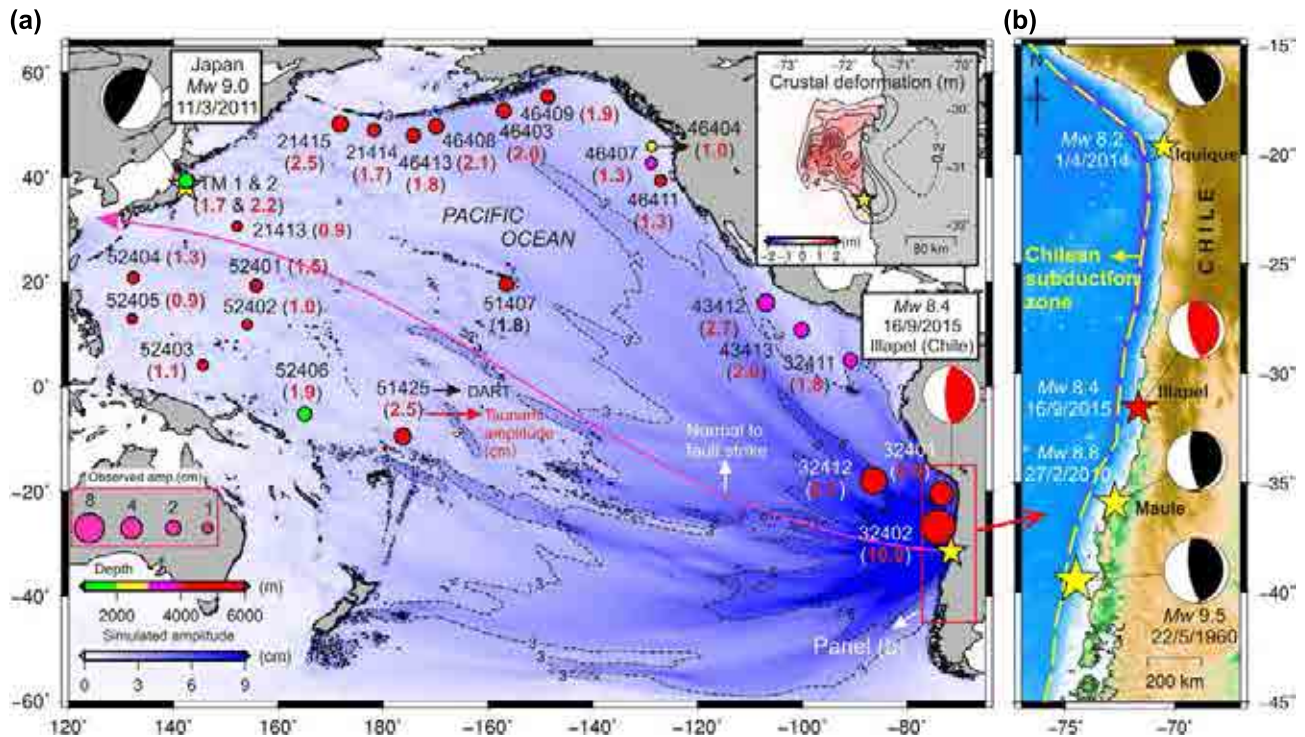
Figure 1. (a) Map of the Pacific Ocean and locations of DARTs used in this study. Dashed contours represent maximum simulated tsunami zero-to-crest amplitudes in cm from our Pacific-wide tsunami simulations for the 2015 Illapel event. The black and red numbers close to each DART represent the DART name and maximum observed zero-to-crest tsunami amplitude in cm. The size of the circles is proportional to the observed tsunami amplitudes, while their colour shows the water depth of the DART sensor. Change of text colour between black and white is for increasing the visual clarity of the text. The panel in the top-right corner is the crustal deformation generated by the 2015 Illapel event based on the source model by Heidarzadeh *et al.* (2016a). (b) Epicentres and magnitudes of past large earthquakes along the Chilean subduction zone.

tating trans-oceanic tsunami that was recorded by a great number of DART stations and by Japanese and Canadian open-ocean cable observatories (Rabinovich & Eblé 2015). The open-ocean records from such a worldwide swarm of great tsunamis are very valuable for studying ocean-wide propagation and deep-ocean properties of tsunamis. Some of the benefits of DART and other open-ocean data are: applications in early tsunami warnings, revealing first negative phases of the tsunami waveforms, and estimation of spectral properties and energy decay of tsunami waves and earthquake source processes (Baba *et al.* 2004, 2014; Saito *et al.* 2010; Løvholt *et al.* 2012; Rabinovich *et al.* 2013; Allgeyer & Cummins 2014; Heidarzadeh & Satake 2014a; Okal *et al.* 2014; Watada *et al.* 2014; Eblé *et al.* 2015; Heidarzadeh *et al.* 2015; Zaytsev *et al.* 2016, 2017). The main purpose of this study is to examine the ocean-wide propagation of the 2015 Illapel tsunami through investigating the DART records and comparing them with other recent trans-oceanic tsunamis. We formulate certain empirical relationships for the durations and amplitudes of initial negative phases of trans-oceanic tsunamis. Furthermore, the concept of empirical Green's functions is applied to reconstruct the source spectrum of the 2010 Maule tsunami by applying spectral deconvolution using the Illapel tsunami as the empirical Green's function.

2 DATA AND METHODOLOGY

The data used in this study are DART records from the Pacific Ocean provided by the US National Oceanic and Atmospheric Administration (NOAA). The DART stations are located at water depths of 1.5–5 km (Fig. 1) and the records had sampling intervals of 1

min as they were the *Event mode* data downloaded from the NOAA website (e.g. Rabinovich & Eblé 2015). The methodology was a combination of: time-series analysis, spectral (Fourier) and wavelet analyses, and numerical simulations. The spectral Fourier analysis reveals the characteristics of the source (i.e. dominating tsunami periods) whereas wavelet analysis demonstrates the temporal changes in these periods. All tsunami records were detided by estimating the tidal signals employing polynomial fitting and then removing them from the original records. The other methods for detiding of DART records are conducting harmonic analysis (e.g. Heidarzadeh & Satake 2013b, 2015; Rabinovich & Eblé 2015) or applying digital filters (e.g. Heidarzadeh & Satake 2014b). It was demonstrated by Heidarzadeh *et al.* (2015) that these detiding methods give very similar results for DART records. For the Fourier analysis, we applied the MATLAB command *Pwelch* which is based on the Welch algorithm (Welch 1967) with Hanning window and 50 per cent of overlaps. The length of the waveform used for Fourier analysis was 3–4 hr which is equivalent to 180–240 data points. For wavelet analysis, we applied the wavelet package by Torrence & Compo (1998) using the *Morlet* mother function with a wavenumber of 6.0 and a wavelet scale width of 0.10.

For tsunami simulations, we applied the shallow-water numerical model by Satake (1995). Linear simulations with time step of 5.0 s were conducted for a total time of 30 hr. The time step follows the Courant stability condition of the Finite Difference computations (Satake 1995). The inundation on dryland was not permitted because the purpose of the tsunami modelling was far-field tsunami propagation and comparison with observed DART data, not estimation of the tsunami run-up. A 5 arcmin bathymetric grid, resampled

Table 1. Source parameters of the earthquake source models used in this study.

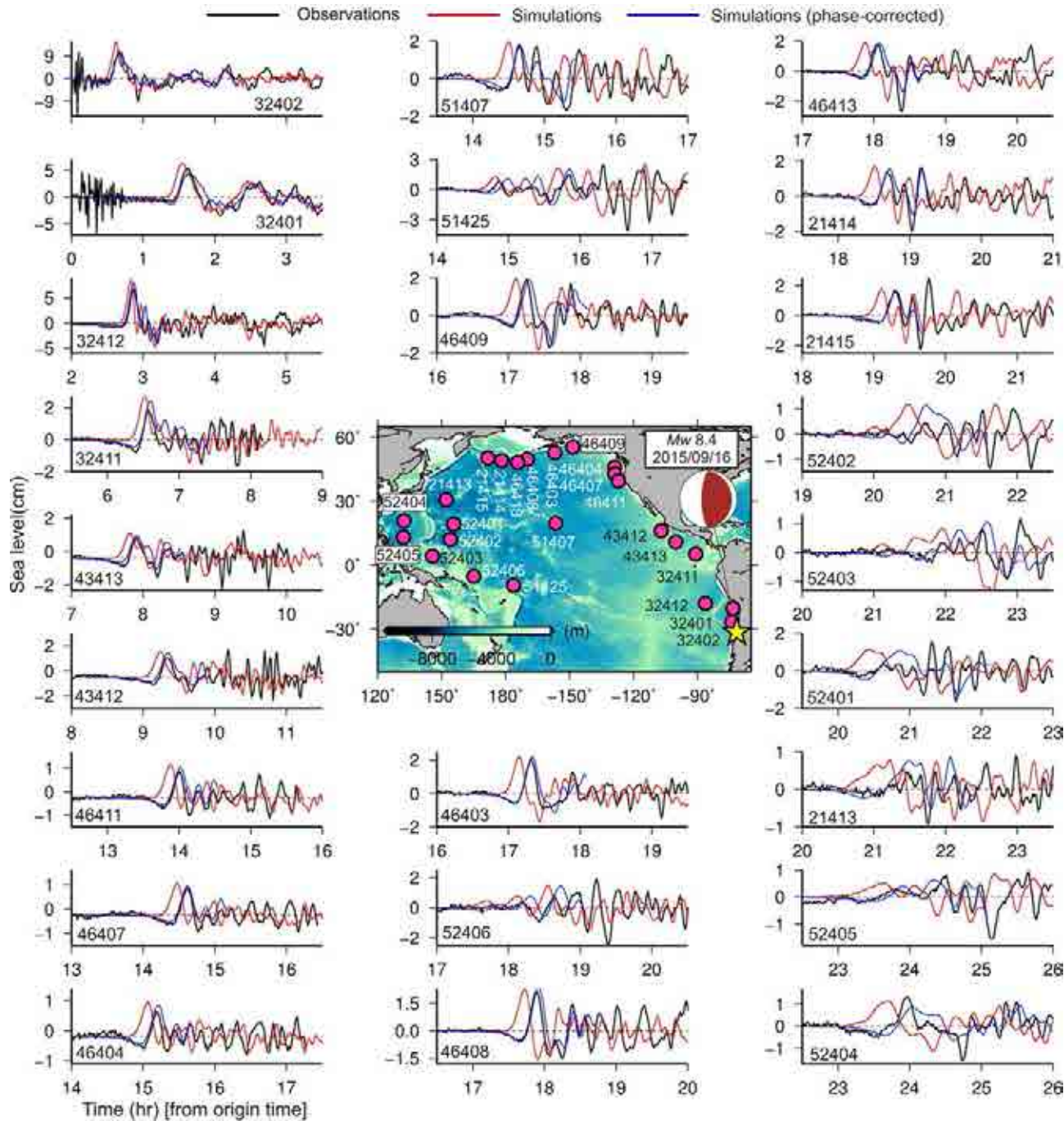| Event name	M_w	Fault dimensions $(L \times W)$[a] (km)	Average slip (m)	Maximum slip (m)	Reference
2014 Iquique	8.2	160 × 140	1.7	7.0	Gusman *et al.* (2015)
2015 Illapel	8.4	200 × 160	2.2	7.1	Heidarzadeh *et al.* (2016a)
2010 Maule	8.8	500 × 150	3.8	18.8	Fujii & Satake (2013)
2011 Tohoku	9.0	550 × 200	9.5	69.1	Satake *et al.* (2013)

[a]Length and width.

Figure 2. The observed (black lines) and simulated (red lines) tsunami waveforms for the 2015 September 16 Illapel tsunami. The blue lines show the corrected waveforms based on the method by Watada *et al.* (2014) that includes the effects of the elastic loading, seawater compressibility and geopotential variations.
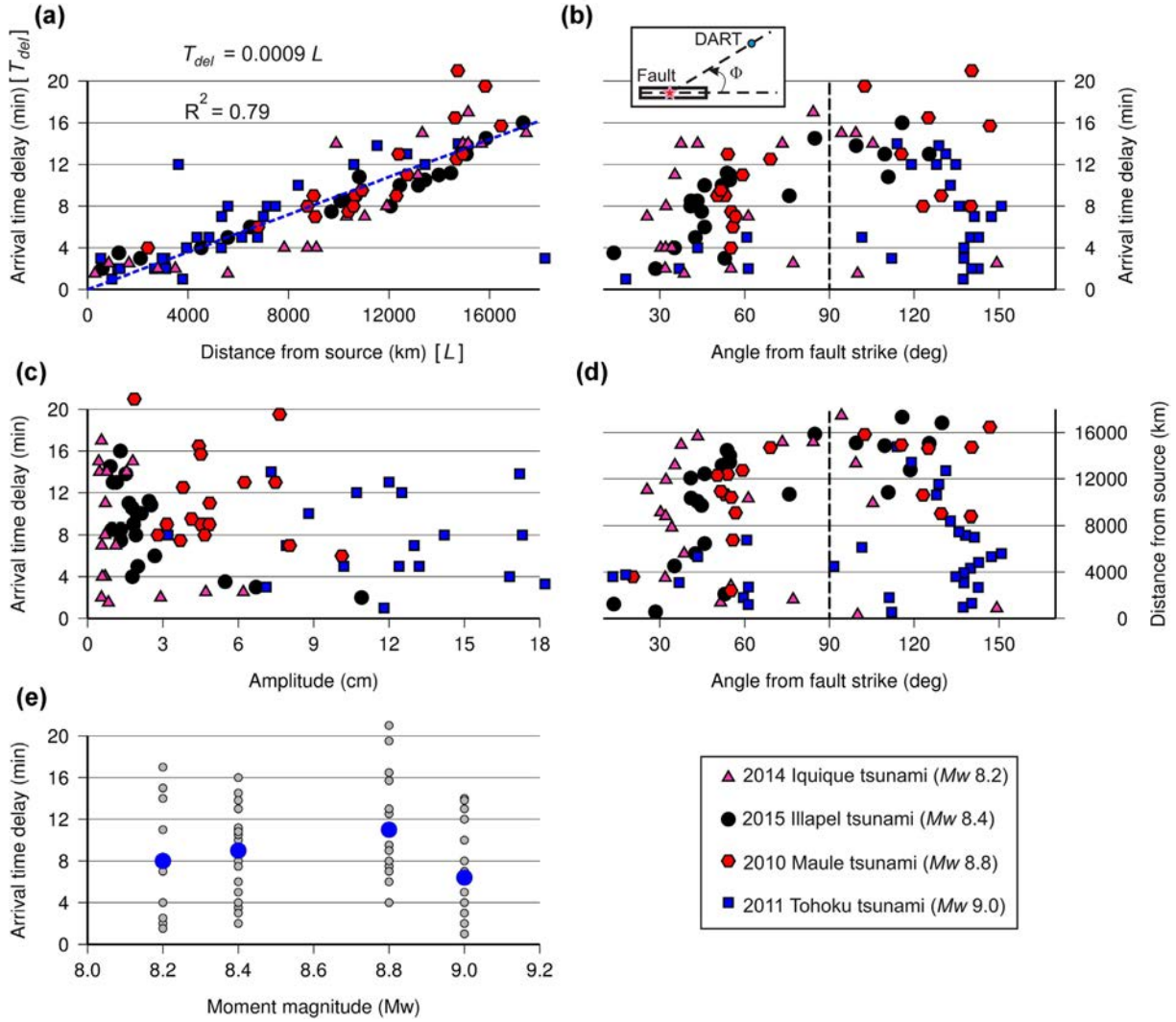
Figure 3. The arrival time delays as functions of the distance from the source (a), the angle from the fault strike (b), the tsunami amplitude (c), and the moment magnitude (e) for four trans-Pacific tsunamis. The relationship between the distance from the source and the angles from the fault strike is shown in (d). The small grey circles in (e) are the available observed arrival time delays for various tsunamis.

from the 30 arcsec GEBCO-2014 bathymetric data (IOC *et al.* 2014; Weatherall *et al.* 2015), was employed for the entire Pacific Ocean. The tsunami source of the 2015 Chile (Illapel) earthquake (M_w 8.4) was the same as that proposed by Heidarzadeh *et al.* (2016a) which includes 96 subfaults each having dimensions of 20 km × 20 km and fault parameters of strike: 5°, dip: 7–23.1°, top depths of subfaults: 9.5–48.2 km, average slip of large-slip area: 5.0 m, and average rake: ∼88°. The vertical crustal deformation for this source model, shown in Fig. 1, was calculated by the analytical formulas of Okada (1985). The source model for the 2010 Maule tsunami was based on that of Fujii & Satake (2013) which includes average and maximum slip values of 3.8 and 18.8 m, respectively, over a fault plane with 36 subfaults (each 50 km × 50 km). The 2014 Iquique source has a maximum slip of 7 m over a fault plane having 63 subfaults (each 20 km × 20 km) (Gusman *et al.* 2015). According to Satake *et al.* (2013), the source size of the 2011 Tohoku tsunami was 550 km (length) × 200 km (width) (over a fault with 55 subfaults; each 50 km × 50 km or 50 km × 25 km) with average and maximum slip values of 9.5 and 69.1 m, respectively. Table 1 presents a summary of the characteristics of various source models used in this study.

3 OBSERVED AND SIMULATED TSUNAMI WAVEFORMS FOR THE 2015 ILLAPEL TSUNAMI

Fig. 2 presents 24 observed DART waveforms (black lines) of the 2015 Illapel tsunami along with the numerically simulated waveforms (red lines). The waveforms for each DART look similar, however, there is a 1–16 min difference in arrival time. A typical feature of many stations (e.g. DARTs 32411, 43413 and 46411 in Fig. 2) is a small negative initial phase, which was not reproduced by the numerical model. These arrival time differences and initial tsunami negative phases were reported for far-field records of other trans-oceanic tsunamis, such as the 2010 Maule, 2011 Tohoku and 2014 Iquique tsunamis (Rabinovich *et al.* 2013; Takagawa 2013; Allgeyer & Cummins 2014; Watada *et al.* 2014; Eblé *et al.* 2015; Heidarzadeh *et al.* 2015). Watada *et al.* (2014) explained these arrival time differences and the reversal of initial phases by the influences of three factors: (1) the elastic loading of the Earth due to tsunami propagation, (2) the compressibility of the seawater, and (3) the geopotential variations associated with the motion of mass.
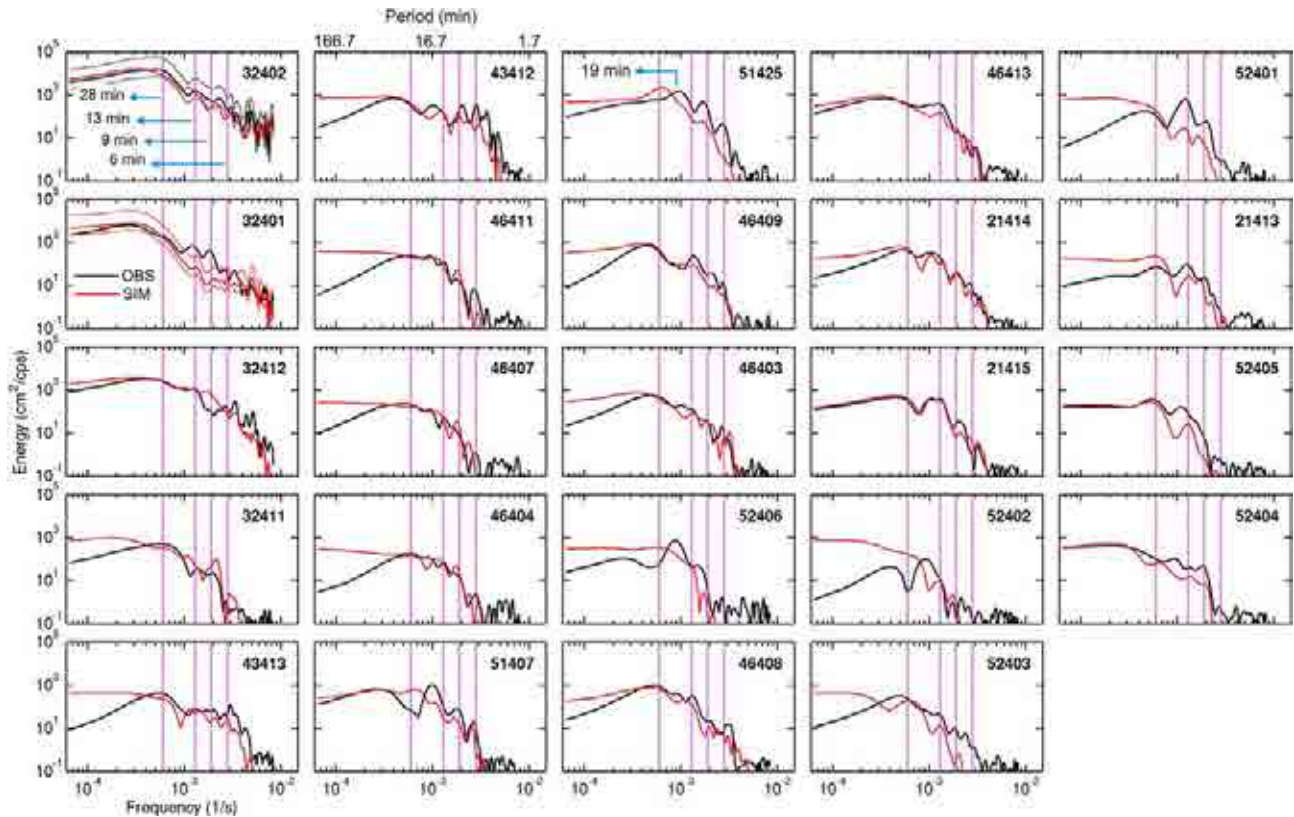
Figure 4. The Fourier analysis for the observed and simulated DART records of the 2015 Illapel tsunami. The dashed black lines for DART 32402 and the dashed red lines for 32401 are examples of the 95% confidence levels for the observation and simulation, respectively.

These three effects had not been considered in our numerical model which was based on shallow-water equations.

To include the effects of the indicated factors in the tsunami simulations, we applied the waveform phase-correction method developed by Watada *et al.* (2014). This method takes into account the fact that tsunami phase velocity is not constant as assumed by the shallow-water theory, but is a function of wave frequency. The method by Watada *et al.* (2014) transforms the simulated waveforms from the time domain to the frequency domain using the Fourier transform and then replaces the phase part of the tsunami spectrum by the corrected phase spectrum. The inverse Fourier transform enables us to restore the phase-corrected time-series (blue lines in Fig. 2). This method takes into account the ocean-water compressibility and the Earth's elasticity and geopotential perturbations to accurately modify the tsunami arrival time delay, as well as its initial phase reversal. Allgeyer & Cummins (2014) applied a different method by including the effects of ocean-water compressibility and seafloor elastic loading in the tsunami simulations and obtained similar results. In most cases, the corrected waveforms are in good agreement with the observations. The exceptions are a few DARTs in the western part of the Pacific Ocean, in particular, DARTs 52401 and 52402; the reason of this disagreement is not quite clear.

4 FAR-FIELD PROPAGATION AND TRAVEL TIMES OF TRANS-PACIFIC TSUNAMIS

To better understand the mechanism of the arrival time differences between observations and shallow-water simulations in the far-field, we plotted these delays against the distances from the source

(Fig. 3a), angles from the fault strike (Fig. 3b), and wave amplitudes (Fig. 3c). A linear relationship is observed between the distance from the source and the arrival time delay in good agreement with the results previously reported by Takagawa (2013); Watada *et al.* (2014) and Heidarzadeh *et al.* (2015) for several other trans-Pacific tsunamis. Our data resulted in the following linear relationship between distance from the source in km (L) and the arrival time delay in minutes (T_{del}) with $R^2 = 0.79$ for the quality of the fit (Fig. 3a):

$$T_{del} = 0.0009 \, L \qquad (1)$$

Theoretically, the arrival time delay should be zero for a distance of zero; therefore, the linear relationship in eq. (1) passes through the origin of the coordinate system. In fact, the 1–2 min delays in the near-field (Fig. 3a) are due to the uncertainties in the travel time measurements. It appears that stations located normal to the fault strike receive longer arrival delays (Fig. 3b). However, the plot of the distance against the angle from fault strike reveals that stations located normal to the fault strike are distal (Fig. 3d). In other words, the observed relationship between the arrival time delay and the angle from the fault in Fig. 3(b) could be due to the distance. According to Figs 3(c)–(e), there is no evident correlation between the arrival time delay and the amplitude or moment magnitude.

5 SPECTRAL ANALYSIS OF THE 2015 ILLAPEL TSUNAMI

Figs 4 and 5 show the results of spectral and wavelet (frequency–time) analyses of the observed and simulated (uncorrected for phase) DART records of the 2015 Illapel tsunami. The spectral analysis reveals four main peaks at periods of approximately 6,
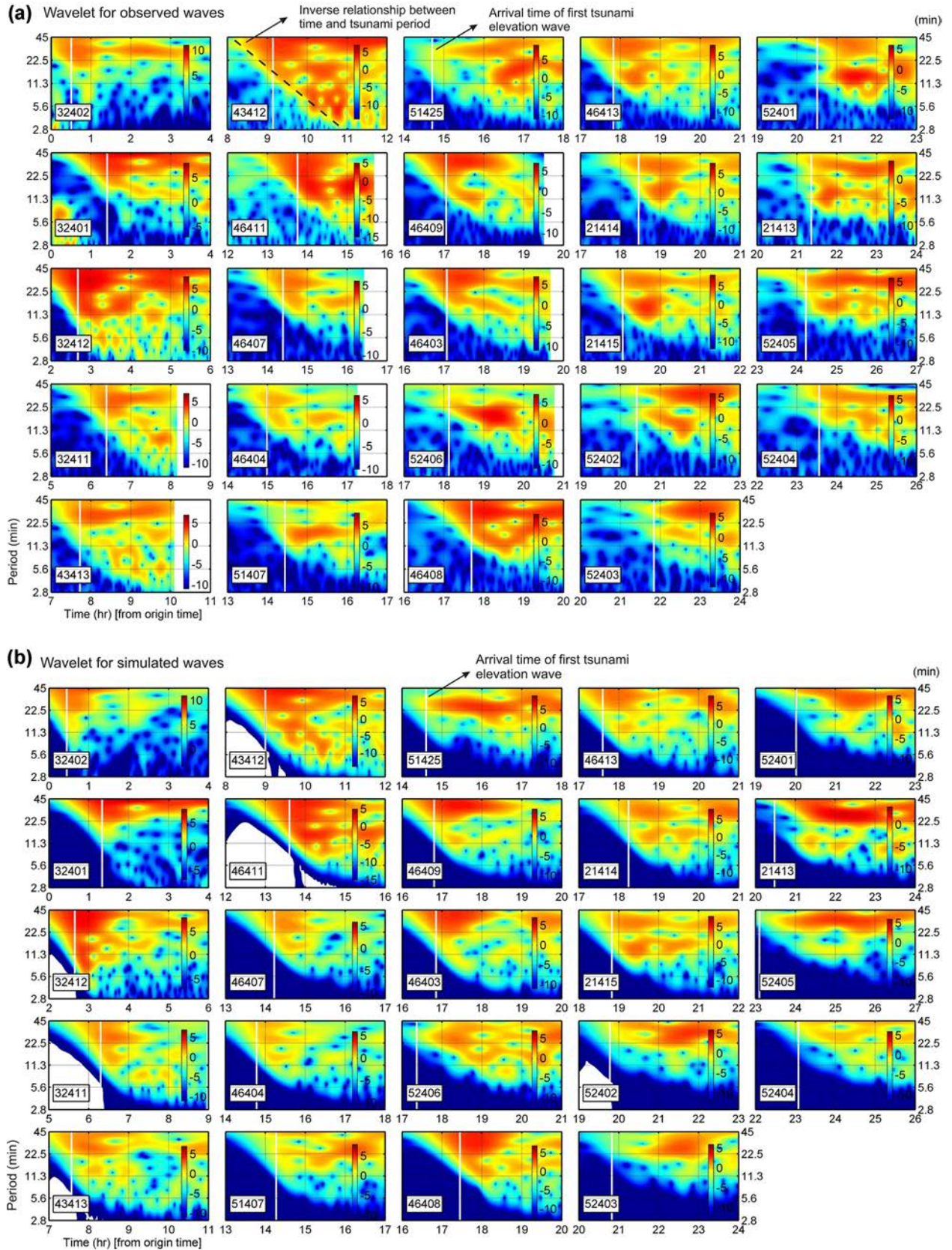
(a) Wavelet for observed waves

(b) Wavelet for simulated waves

Figure 5. The frequency-time (wavelet) analyses for observed (a) and simulated (b) DART records of the 2015 Illapel tsunami.
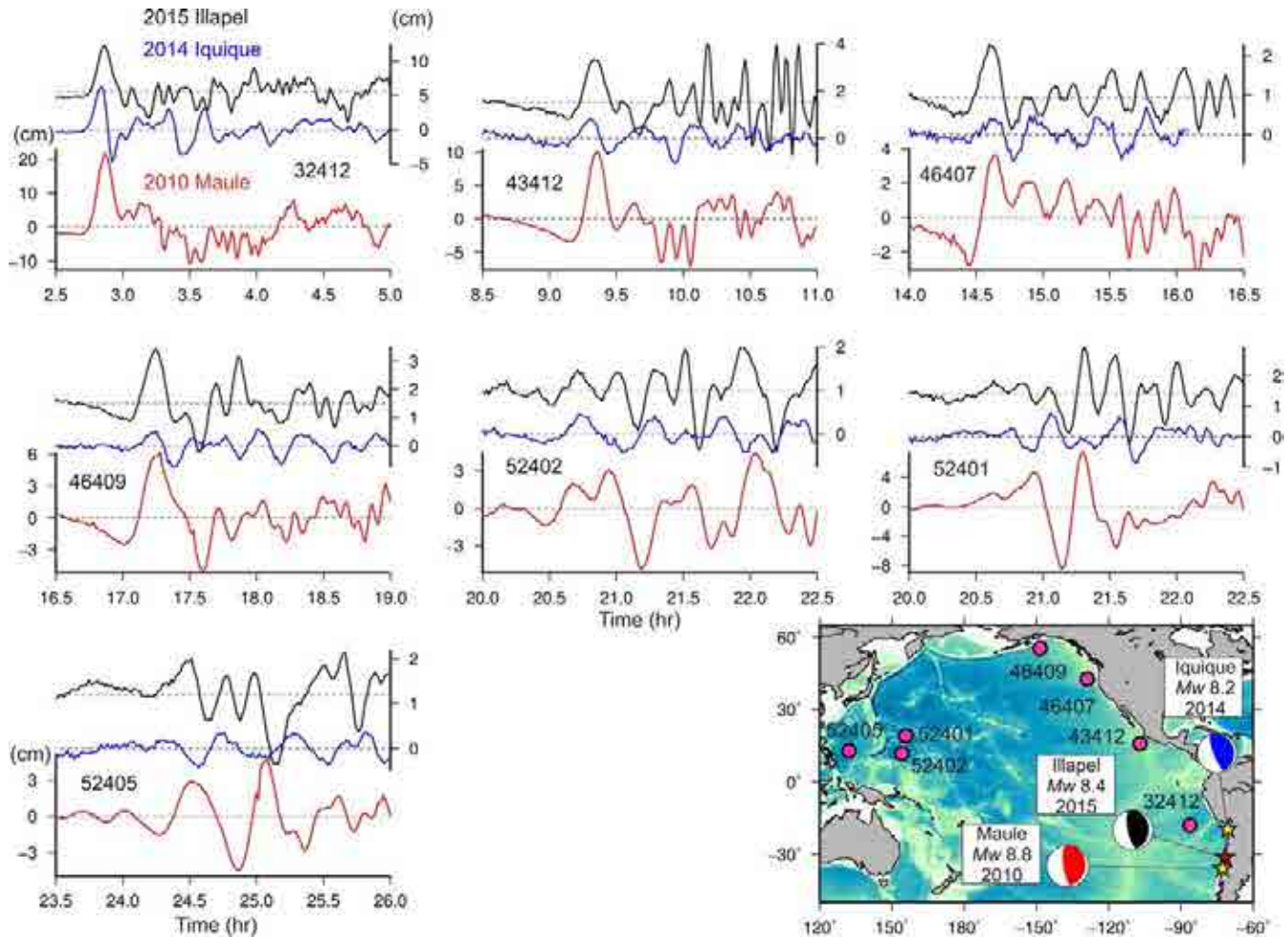
Figure 6. Tsunami waveforms from three recent major tsunamis generated offshore of Chile recorded at DART stations. The time axis is shifted to align the waveforms at their first peak amplitude.

9, 13 and 28 min (Fig. 4). The two latter peaks (13 and 28 min) are stronger and appear at most stations. Four stations of 52406, 52402, 51425 and 51407 show a single dominating period at ∼19 min (Fig. 4). Distribution of tsunami energy over frequency and time domains reveals that the aforesaid four peak periods show non-stationary behaviour over time. A combination of Fourier and wavelet results may favour the two periods of ∼13 and ∼28 min as prevailing tsunami periods. Wavelet analysis reveals certain energy at periods >30 min before the arrival times of the first elevation wave (e.g. DARTs 32412, 43412, 46403 and 46408) (Fig. 5). In most wavelet plot, an inverse relationship between the time and wave period is observed (in both observations, Fig. 5a, and simulations, Fig. 5b) which shows shorter-period waves appear in DART stations later than longer-period waves (the dashed-line in Fig. 5a in 43412). This behaviour is also evident from the time-series of the tsunami waveforms in Fig. 2, where in most records the first few waves are longer than the later waves. As compared to the other two large tsunamis off Chile, the dominating period band of the Illapel tsunami (13–28 min) was longer than that from the 2014 Iquique tsunami (14–21 min, after Heidarzadeh *et al.* 2015), and shorter than the 2010 Maule tsunami (12–50 min, after Rabinovich *et al.* 2013). The 2011 Tohoku tsunami showed two dominating periods at 37 and 67 min, according to Heidarzadeh & Satake (2013a).

These results and periods are in good agreement with those found by Zaytsev *et al.* (2016, 2017) based on the analysis of DART records of the 2010, 2011, 2014 and 2015 tsunamis offshore of Mexico.

6 COMPARISON OF THE TSUNAMI WAVEFORMS FROM CHILEAN TRANS-PACIFIC TSUNAMIS

Tsunami waveforms from three recent major Chilean tsunamis are shown in Fig. 6 for seven DART stations. The time axis is shifted to align the waveforms at their first peak amplitude. It can be seen that the waveforms from the Illapel tsunami look similar to those from the Maule tsunami, whereas those from the Iquique event are clearly different from the aforesaid two tsunamis (Fig. 6). This is possibly because the epicentres of the Illapel and Maule earthquakes are close to each other (Fig. 6); hence, the resulting tsunamis propagated similar tracks to reach the DART stations. The amplitudes of the Maule tsunami are 2–5 times larger than those of the Illapel (Fig. 6). Since the Illapel earthquake (M_w 8.4) was smaller than the Maule (M_w 8.8), the former event may serve as an empirical Green's function for the latter earthquake (e.g. Heidarzadeh *et al.* 2016b).
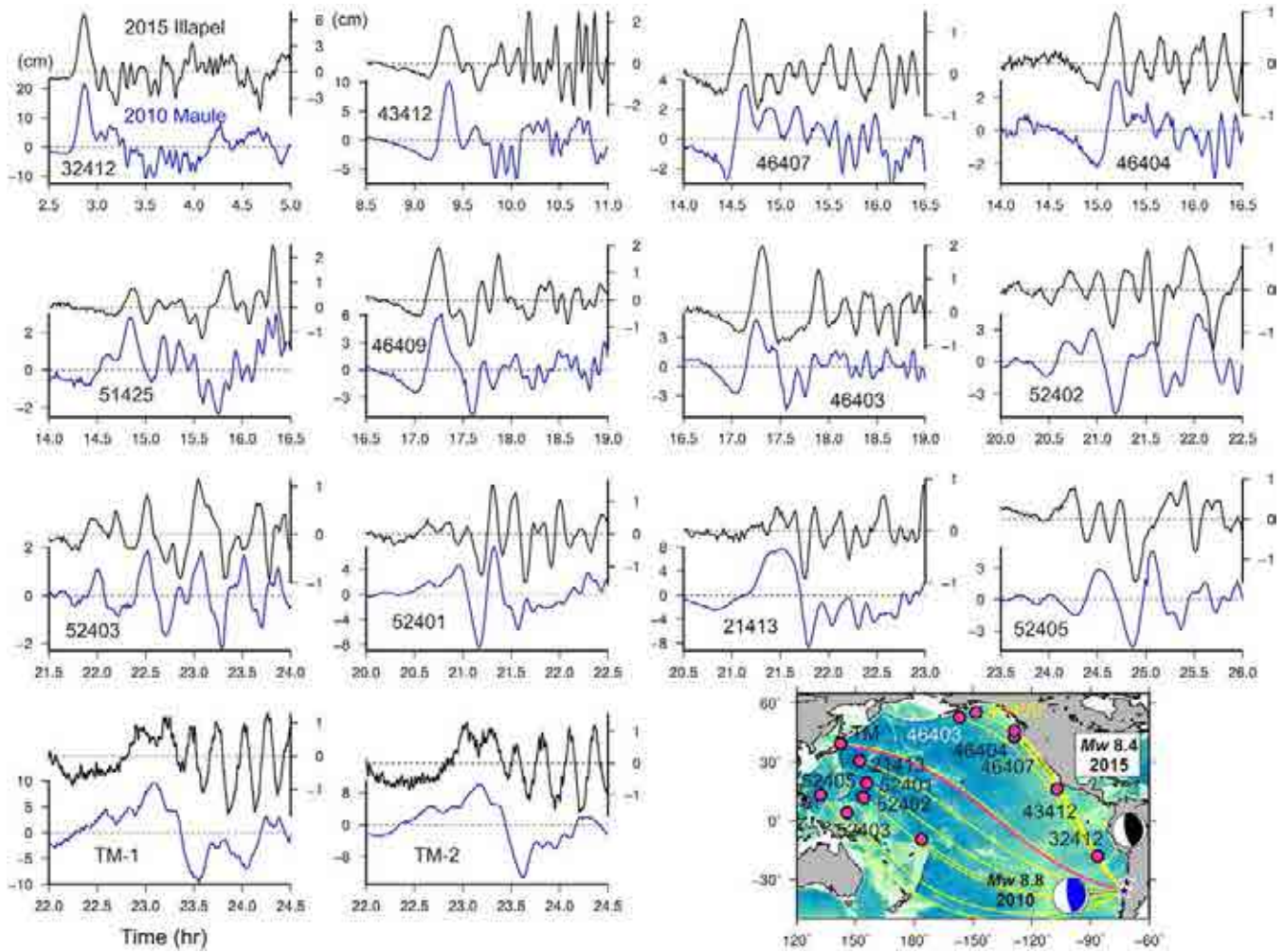
Figure 7. DART tsunami waveforms from the 2015 Illapel and 2010 Maule tsunamis.
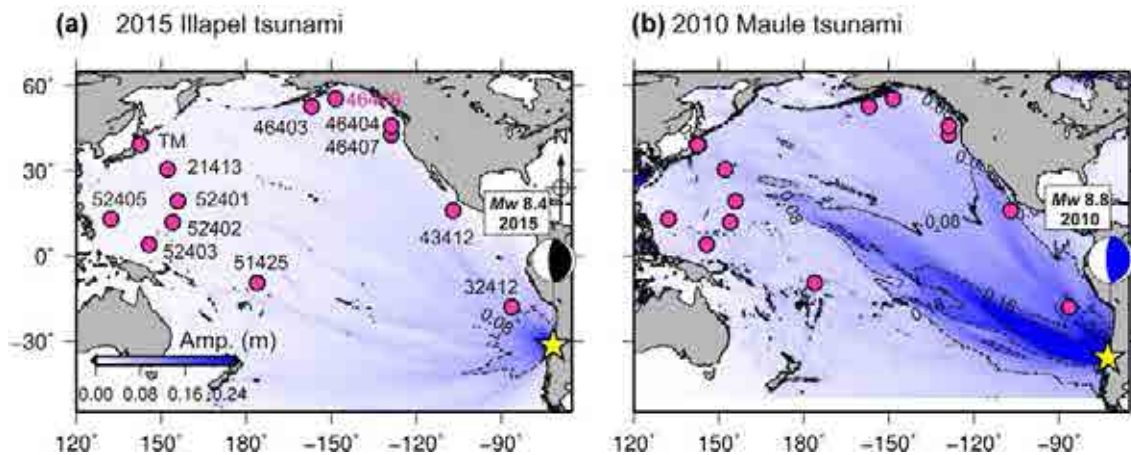

Figure 8. Maximum simulated tsunami amplitudes for the 2015 Illapel (a) and 2010 Maule (b) tsunamis.

7 EMPIRICAL GREEN'S FUNCTIONS FOR THE CHILEAN TSUNAMIS

The concept of empirical tsunami Green's function was formulated and successfully applied to the 2013 Santa Cruz tsunami by Heidarzadeh *et al.* (2016b). This concept, which is akin to a similar approach in seismology, postulates that for two tsunamis occurring close to each other, the smaller event can be considered as an empirical Green's function to be used to remove the non-source effects from the spectrum of the larger tsunami. According to Heidarzadeh *et al.* (2016b), spectral deconvolution, conducted by dividing the spectrum of the larger event by that of the smaller event, gives the source spectrum of the larger tsunami. This approach is close to the idea of Rabinovich (1997) where the background spectrum is
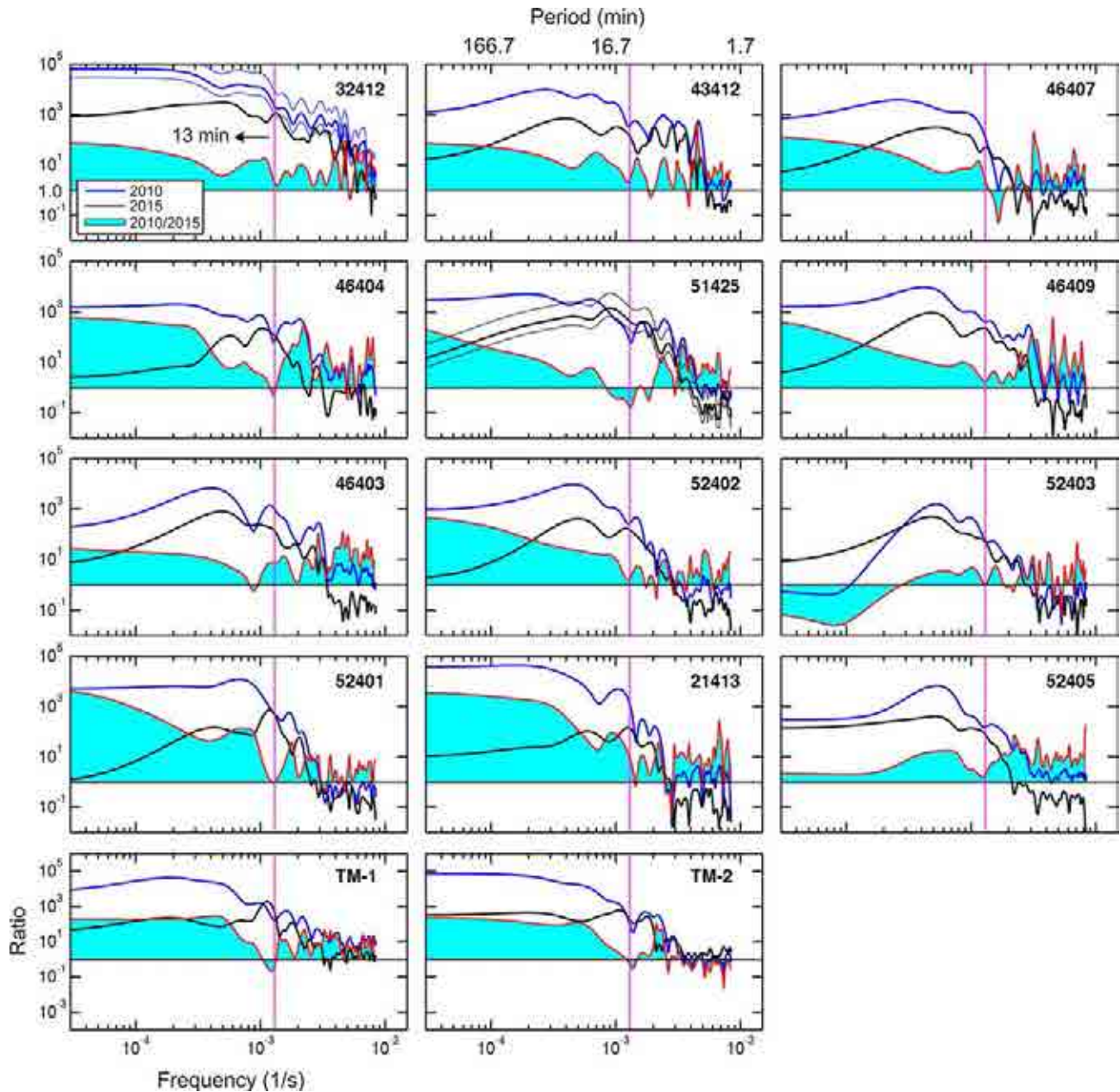
Figure 9. Spectral ratios for DART records of the 2015 Illapel and 2010 Maule tsunamis. The dashed blue lines for DART 32412 and the dashed black lines for 51425 are examples of the 95 per cent confidence levels for the 2010 Maule and 2015 Illapel tsunamis, respectively.

used to suppress the influence of topography and to restore the original tsunami spectrum. Heidarzadeh *et al.* (2016b), by applying this concept on the 2013 (M_w 8.0) and 2015 (M_w 8.0) Solomon Island tsunamigenic earthquakes, obtained a source period band of 10−22 min for the 2013 Solomon Island tsunami.

Here, the epicentres of the Maule and Illapel events are close to each other (Fig. 7), while the energy released by the former earthquake is ∼4 times larger than that of the latter. Therefore, the Illapel tsunami can be used as the empirical Green's function for the Maule event. The ocean-wide DART records of the two events are compared in Fig. 7, while their basin-wide distribution of tsunami amplitudes is shown in Fig. 8. The DART waveforms of the two events look similar, although the amplitudes of the Maule tsunami are 2–5 times larger than those of the Illapel event. The

spectral ratios in Fig. 9 (shaded spectra) are the results of the spectral deconvolution and reveal the source spectra of the Maule tsunami, which is in the period range of 13–50 min (Fig. 9). The bottom limit of this period range, that is 13 min, is the period that gives a spectral ratio of ∼1 and the upper limit, that is 62 min, is the period that most of the ratios become either flat or ∼1.0. This tsunami source period band is close to that of 12–50 min previously reported by Rabinovich *et al.* (2013) and Zaytsev *et al.* (2016) which was calculated by the direct Fourier analysis of the Maule tsunami waveforms. For comparison, the source periods of other tsunami events worldwide are: 20–90 min for the 2011 Tohoku tsunami (Heidarzadeh & Satake 2014a; Zaytsev *et al.* 2017) and 2–30 min for the 2017 Bodrum–Kos (Turkey–Greece) tsunami (Heidarzadeh *et al.* 2017).
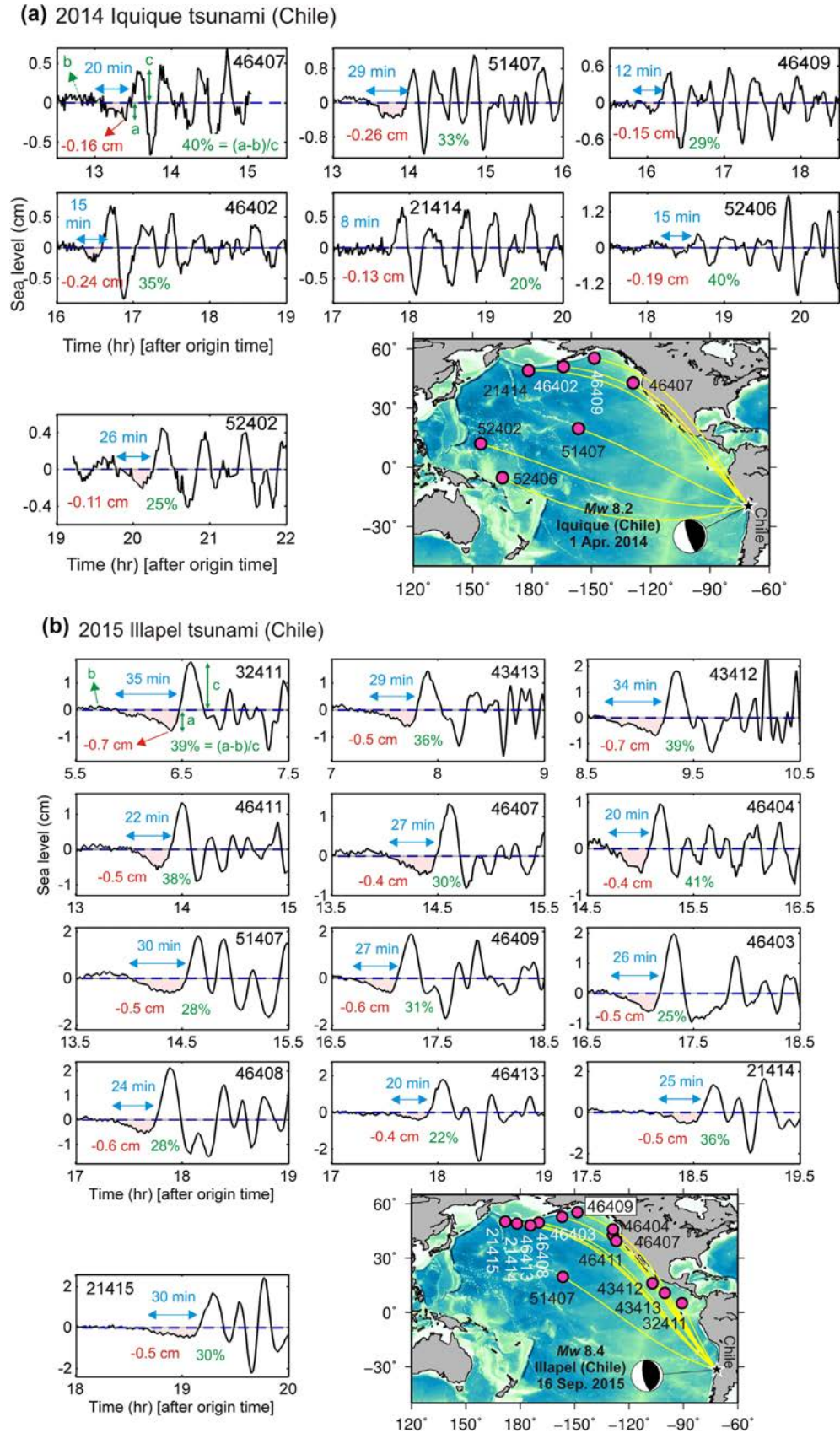
Figure 10. Characteristics of the initial negative phases recorded at DART stations for (a): the Iquique tsunami; (b): the Illapel tsunami; (c): the Maule tsunami; and (d): the Tohoku tsunami. Parameters "a", "b" and "c" are: the maximum amplitude of the initial negative phase, the maximum noise amplitude before the tsunami arrival, and the maximum amplitude of the first frontal crest wave, respectively.

Figure 10. continued.

Figure 11. (a) The durations, (b) amplitudes; and (c) amplitude ratios of the initial phases as functions of distances of the DART stations from the source. (d), (e) and (f) are the same parameters as functions of the earthquake moment magnitude (M_w). Parameters "a", "b" and "c" are: the maximum amplitude of the initial negative phase, the maximum noise amplitude before the tsunami arrival, and the maximum amplitude of the first 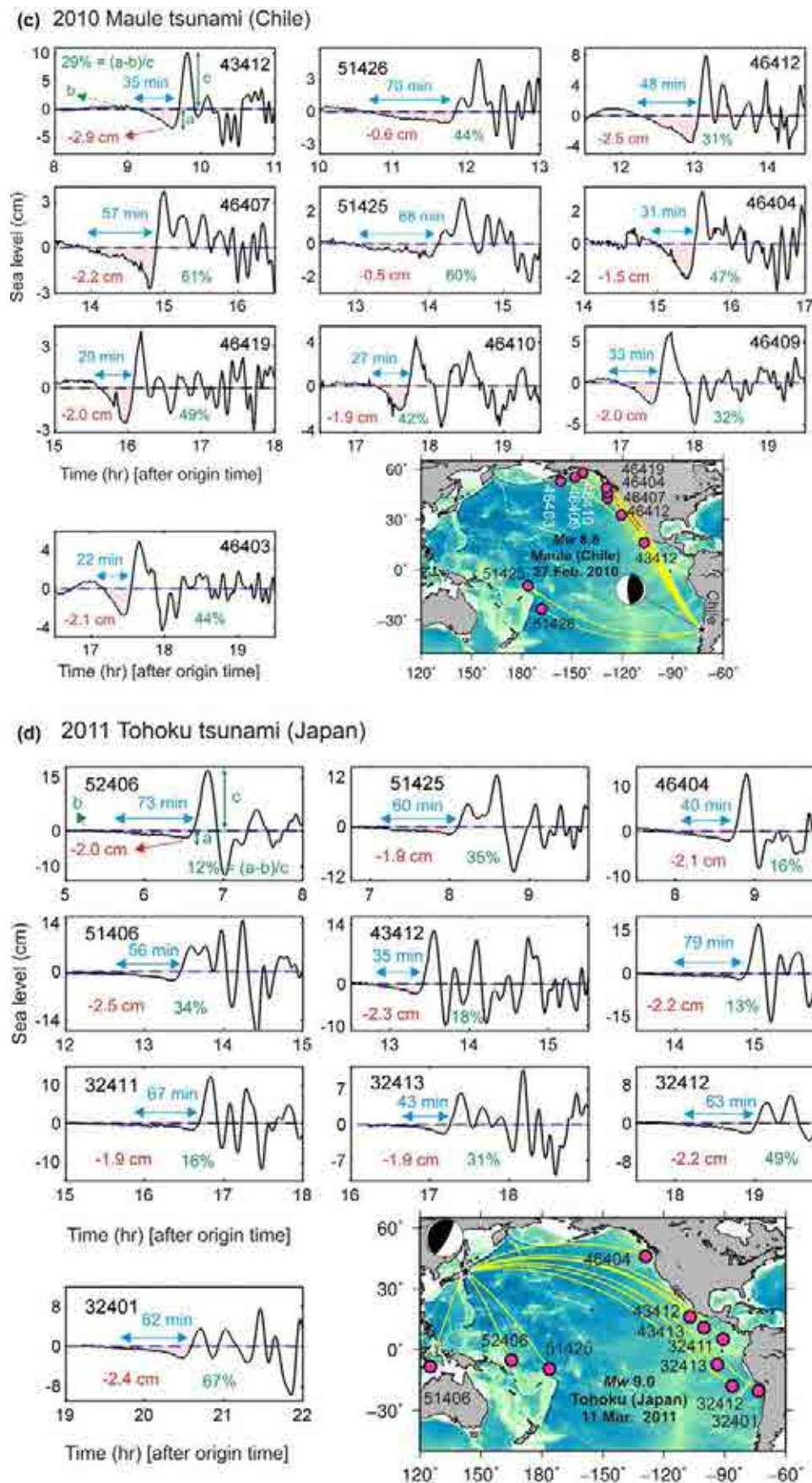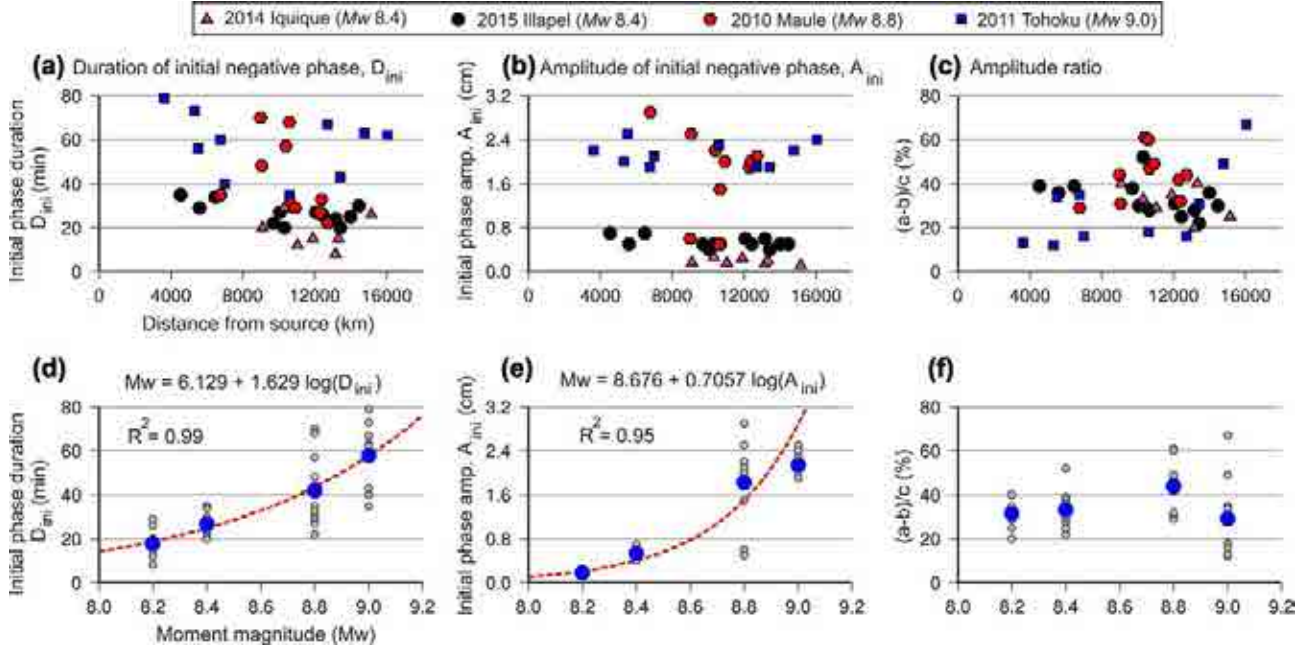frontal crest wave, respectively. The small grey circles in panels (d), (e) and (f) indicate the data available from DART observations for various tsunamis.

8 CHARACTERISTICS OF THE INITIAL NEGATIVE PHASES FOR TRANS-PACIFIC TSUNAMIS

Fig. 10 shows the maximum amplitude and duration of the observed initial negative phases at DART stations for the four trans-Pacific tsunamis. Here, the duration of the initial phase is defined as the time interval between the beginning of the sea level recession relative to the mean sea level (the initiation of the negative phase) and the time that it reaches the mean sea level again. For the present analysis, the DART data with relatively high signal-to-noise ratios were selected to achieve reliable results (Fig. 10). The durations of the initial phase (D_{ini}) were 8–29, 20—35, 22–70 and 40–79 min for the Iquique, Illapel, Maule and Tohoku tsunamis, respectively (blue values in Fig. 10). The maximum negative amplitudes of the initial phases (A_{ini}) were 0.11–0.26, 0.4–0.7, 0.5–2.9 and 1.9–2.5 cm for these tsunami, respectively (red values in Fig. 10), while the amplitude ratios of the negative phases relative to the amplitude of the first elevation wave were 20–40 per cent, 22–41 per cent, 29–61 per cent and 12–67 per cent, respectively (green values in Fig. 10). The amplitudes of the initial phase were significant as compared to the frontal elevation tsunami amplitudes.

Figs 11(a)–(c) shows the durations, the amplitudes, and the amplitude ratios of the initial phases as a function of distances of the DART stations from the source for the four trans-Pacific tsunamis. Neither of them show evident trend with distance. Figs 11(d)–(f) shows their variations with the earthquake moment magnitudes. The durations and amplitudes of the initial negative phases indicate obvious dependence on the earthquake magnitudes, while the amplitude ratios do not. Our results yield the following two equations for the relationship between the properties of the initial phases (i.e. D_{ini} and A_{ini}) and M_w (Figs 11d and e):

$$M_w = 6.129 + 1.629 \log (D_{ini}) \tag{2}$$

$$M_w = 8.676 + 0.706 \log (A_{ini}) \tag{3}$$

in which, log is the logarithm to the base 10, D_{ini} is in min, A_{ini} is in cm and the qualities of fit are $R^2 = 0.99$ and $R^2 = 0.95$ for eqs (2) and (3), respectively (Fig. 11 and Table 2). A linear relationship between M_w and A_{ini} yields a slightly higher R^2 value (i.e. 0.986), whereas between M_w and D_{ini} it is slightly smaller ($R^2 = 0.98$). Here, we chose the logarithmic equations for two reasons: first, traditionally the relationship between earthquake magnitude (M_w) and seismic/tsunami wave amplitudes is expressed in logarithmic forms (e.g. Gutenberg & Richter 1954; Abe 1979) and, second, the quality of fit between the linear and logarithmic equations was very similar in our analysis. It should be noted that the M_w values are usually reported with one decimal place; therefore, the M_w values obtained from eqs (2) and (3) need to be rounded to one decimal place.

9 DEEP-OCEAN TSUNAMI AMPLITUDES FOR TRANS-PACIFIC TSUNAMIS

Distribution of deep-ocean tsunami zero-to-crest amplitudes from DART stations throughout the Pacific Ocean are shown in Figs 12–13 for four tsunamis. By excluding stations located in the distances <20 arcdeg (2200 km) from the epicentre, the mean amplitudes of 0.9, 1.7, 6.0 and 15.0 cm were obtained for the Iquique, Illapel, Maule and Tohoku tsunamis, respectively (Figs 12a–d). By taking into account the moment magnitudes of these earthquakes (M_w 8.2, 8.4, 8.8 and 9.0, respectively), we can describe the relationship between the earthquake moment magnitude (M_w) and deep-ocean tsunami amplitude (A_{tsu}) by an exponential function (Fig. 13). The resulting equation is:

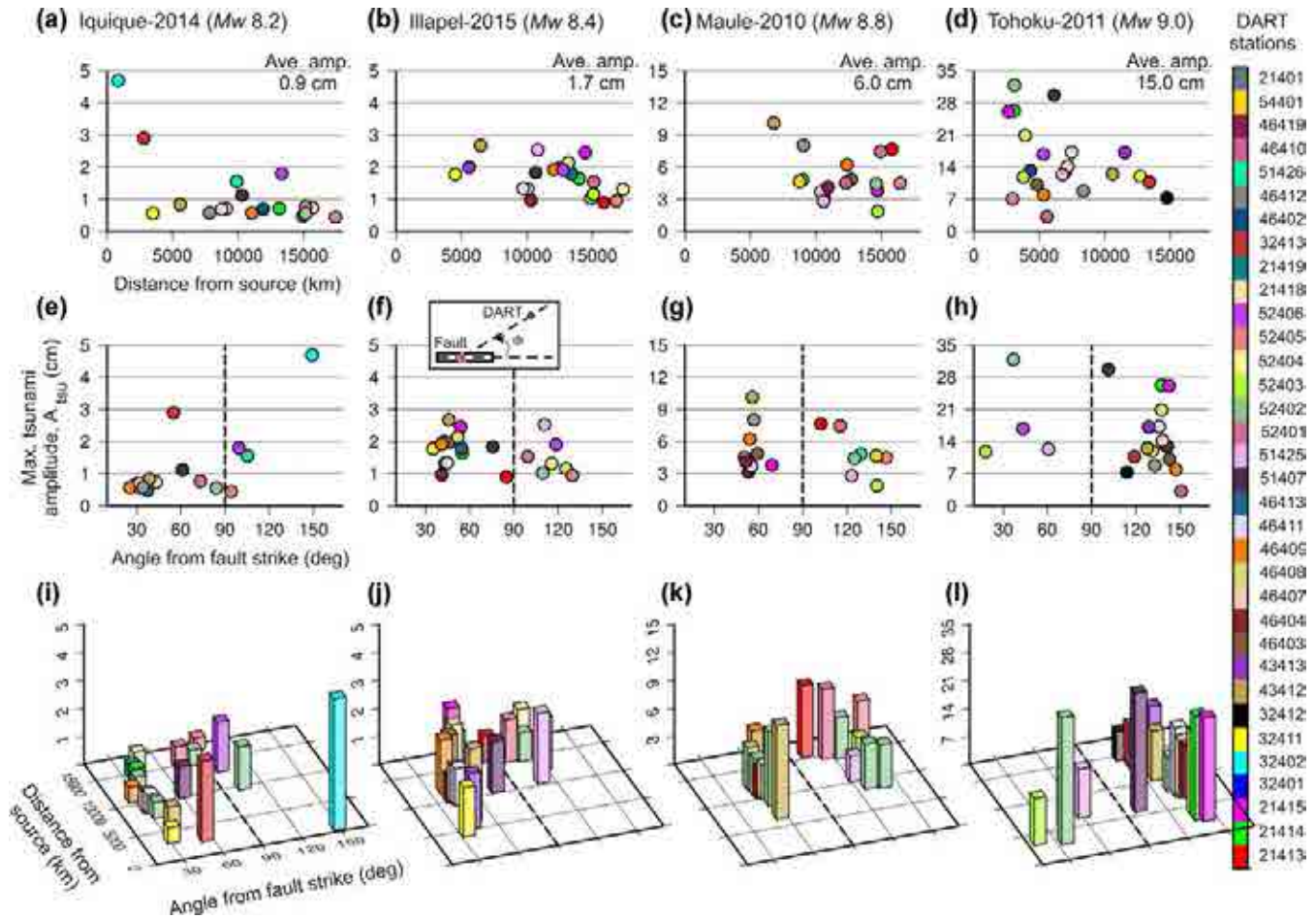$$M_w = 8.245 + 0.665 \log (A_{tsu}) \tag{4}$$

Figure 12. (a–d): Deep-ocean tsunami zero-to-crest amplitudes for four recent trans-Pacific tsunamis as a function of distance from the source. The average values are calculated by excluding stations located at distances <20 arcdeg (2200 km). Distances are based on the great-circle system. (e–h): Deep-ocean tsunami zero-to-crest amplitudes as functions of the angle from the fault strike as shown in the inset in panel f. (i–l): The 3-D-plots showing deep-ocean tsunami zero-to-crest amplitudes as functions of the distances from the source epicentre and angles from the fault strike.
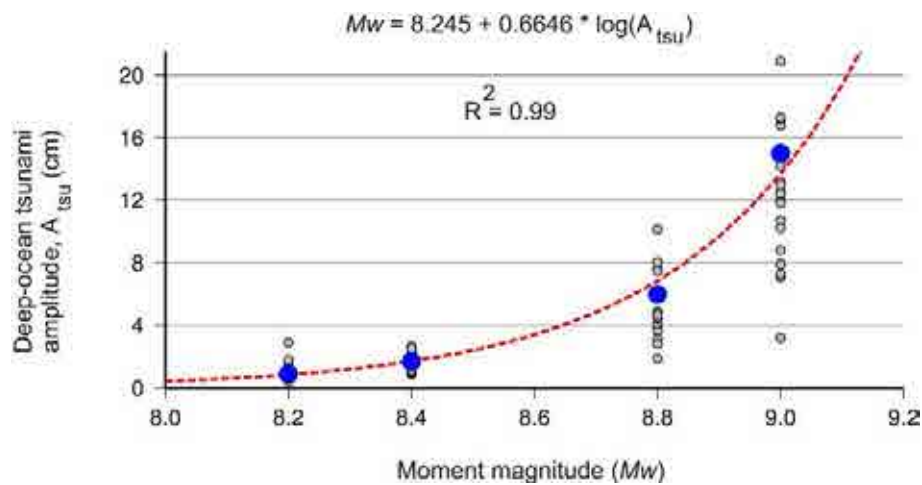

Figure 13. Deep-ocean tsunami amplitudes (A_{tsu}) as a function of the moment magnitude (M_w). The small grey circles indicate the data available from DART observations for various tsunamis.

Table 2. The equations relating duration (D_{ini}) and amplitude (A_{ini}) of the initial negative phase, as well as the mean far-field deep-ocean amplitudes (A_{tsu}) to the earthquake magnitude (M_{w}).

			95% confidence bound		
Equation*	a	b	a	b	R^2
$M_{\text{w}} = a + b \log(D_{\text{ini}})$	6.129	1.629	5.304–6.955	1.089–2.169	0.99
$M_{\text{w}} = a + b \log(A_{\text{ini}})$	8.676	0.706	8.449–8.902	0.202–1.210	0.95
$M_w = a + b \log(A_{tsu})$	8.245	0.665	8.133–8.356	0.509–0.820	0.99

*In these equations, D_{ini} is in min and A_{ini} and A_{tsu} are in cm.

in which, log is the logarithm to the base 10 and A_{tsu} is the deep-ocean tsunami amplitude in cm recorded at distances <20 arcdeg (2200 km) from the epicentre. The quality of fit is $R^2 = 0.99$ (Table 2), indicating that the equation fits very well to the measured data.

There is no evident correlation between the deep-ocean amplitudes and distances from the source (Figs 12a–d). To examine the possible effect of source directivity on far-field tsunami amplitudes, we plotted these amplitudes against the angles from the fault strike (Figs 12e–h), but have not also found any correlation between these two parameters. Considering the fact that the effect of directivity on the far-field wave amplitude is well-established, the reason why such an effect cannot be seen here can be attributed to the sparsity of the DARTs over the entire Pacific Ocean and to the irregular bathymetry of the Pacific Basin. Tsunami waves pass through complicated bathymetric features which scatter tsunami energy and waves or trap the waves (Hébert *et al*. 2001; Heidarzadeh *et al*. 2016b). 3-D plots of the deep-ocean amplitudes versus distance and angle from the fault strike (Figs 12i–l) also does not show any meaningful correlation between these parameters. Assuming a constant value of M_{w}, we can formulate the relationship between A_{tsu} and A_{ini}:

$$A_{\text{ini}} = 0.245 \, A_{\text{tsu}}^{0.9418} \tag{5}$$

Eq. (5) indicates that the amplitude of the initial negative phase (A_{ini}) is approximately 25 per cent of that of the amplitude of the first elevation wave (A_{tsu}), which is in agreement with our observations presented in Section 8.

10 CONCLUSIONS

Ocean-wide and deep-ocean characteristics of the tsunami generated by the 2015 September 16 Illapel earthquake (M_{w} 8.4) were examined based on the DART records from the entire Pacific Ocean and compared with those of three other trans-Pacific tsunamis generated by the 2014 Iquique (M_{w} 8.4), 2010 Maule (M_{w} 8.8) and 2011 Tohoku (M_{w} 9.0) earthquakes. The main findings are:

(1) An arrival time difference of up to 16.0 min was detected between the observed and shallow-water simulated waveforms for the 2015 Illapel tsunami; this difference was resolved using a phase-correction technique. The dominant period band of this tsunami was 13–28 min, which is longer than that of the Iquique tsunami (14–21 min) and shorter than the Maule tsunami (12–50 min).

(2) The waveforms from the 2015 Illapel tsunami looked very similar to those from the 2010 Maule tsunami, although the amplitudes of the 2010 tsunami were approximately 2–5 times larger than of the 2015 tsunami. The Illapel tsunami was used as an empirical Green's function to reconstruct the Maule tsunami and yielded quite reasonable results; the reconstructed source period band of 13–62 min for the Maule event is in a good agreement with the observations.

(3) The duration of the initial negative phases (D_{ini}) was 8–29, 20–35, 22–70 and 40–79 min for the 2014 Iquique, 2015 Illapel, 2010 Maule and 2011 Tohoku tsunamis, respectively. The maximum negative amplitudes of the initial phases (A_{ini}) were 0.11–0.26, 0.4–0.7, 0.5–2.9 and 1.9–2.5 cm for the aforesaid tsunamis, respectively, while the amplitude ratios of the negative phases to the first waves were 20–40 per cent, 22–41 per cent, 29–61 per cent and 12–67 per cent for these tsunamis, respectively. Our results yield the relationships between the initial phase parameters (D_{ini} in min and A_{ini} in cm) and earthquake moment magnitudes (M_{w}) as: $M_w = 6.129 + 1.629 \log(D_{\text{ini}})$ and $M_{\text{w}} = 8.676 + 0.706 \log(A_{\text{ini}})$.

(4) The mean far-field deep-ocean amplitudes (A_{tsu}) for the Iquique, Illapel, Maule and Tohoku tsunamis were 0.9, 1.7, 6.0 and 15.0 cm, respectively. No correlation was found between the deep-ocean amplitudes and distance from the source or angle from fault strike. The relationship between A_{tsu} (in cm) and M_{w} can be described as $M_{\text{w}} = 8.245 + 0.665 \log(A_{\text{tsu}})$.

REFERENCES

Abe, K., 1979. Size of great earthquakes of 1837–1974 inferred from tsunami data, *J. geophys. Res.,* **84**(B4), 1561–1568.

Allgeyer, S. & Cummins, P., 2014. Numerical tsunami simulation including elastic loading and seawater density stratification, *Geophys. Res. Lett.,* **41**(7), 2368–2375.

Baba, T., Hirata, K. & Kaneda, Y., 2004. Tsunami magnitudes determined from ocean-bottom pressure gauge data around Japan, *Geophys. Res. Lett.,* **31**(8), doi:10.1029/2003GL019397.

Baba, T., Takahashi, N. & Kaneda, Y., 2014. Near-field tsunami amplification factors in the Kii Peninsula, Japan for Dense Oceanfloor Network for Earthquakes and Tsunamis (DONET), *Mar. Geophys. Res.,* **35**(3), 319–325.

Eblé, M.C., Mungov, G.T. & Rabinovich, A.B., 2015. On the leading negative phase of major 2010–2014 tsunamis, *Pure appl. Geophys.,* **172**(12), 3493–3508.

Filloux, J.H., 1982. Tsunami recorded on the open ocean floor, *Geophysical Research Letters,* **9**(1), 25–28.

Fujii, Y. & Satake, K., 2013. Slip distribution and seismic moment of the 2010 and 1960 Chilean earthquakes inferred from tsunami waveforms and coastal geodetic data, *Pure appl. Geophys.,* **170**(9-10), 1493–1509.

González, F.I., Mader, C.L., Eble, M.C. & Bernard, E.N., 1991. The 1987–88 Alaskan bight tsunamis: deep ocean data and model comparisons, *Nat. Hazards* **4**(2), 119–139.

Gusman, A.R., Murotani, S., Satake, K., Heidarzadeh, M., Gunawan, E., Watada, S. & Schurr, B., 2015. Fault slip distribution of the 2014 Iquique, Chile, earthquake estimated from ocean-wide tsunami waveforms and GPS data, *Geophys. Res. Lett.,* **42**(4), 1053–1060.

Gutenberg, B & Richter, C.F., 1954. *Seismicity of the Earth and Associated Phenomena,* 2nd edn, Princeton University Press.

Heidarzadeh, M., Harada, T., Satake, K., Ishibe, T. & Gusman, A., 2016b. Comparative study of two tsunamigenic earthquakes in the Solomon Islands: 2015 Mw 7.0 normal-fault and 2013 Santa Cruz Mw 8.0 megathrust earthquakes, *Geophys. Res. Lett.,* **43**(9), 4340–4349.

Heidarzadeh, M., Murotani, S., Satake, K., Ishibe, T. & Gusman, A.R., 2016a. Source model of the 16 September 2015 Illapel, Chile *Mw* 8.4 earthquake based on teleseismic and tsunami data, *Geophys. Res. Lett.,* **42**, doi:10.1002/2015GL067297.

Heidarzadeh, M., Necmioglu, O., Ishibe, T. & Yalciner, A.C., 2017. Bodrum-Kos (Turkey-Greece) Mw 6.6 earthquake and tsunami of 20 July 2017: a test for the Mediterranean tsunami warning system, *Geosci. Lett.,* **4**, 31.

Heidarzadeh, M. & Satake, K., 2013a. Waveform and spectral analyses of the 2011 Japan tsunami records on tide gauge and DART stations across the Pacific Ocean, *Pure appl. Geophys.,* **170**(6), 1275–1293.

Heidarzadeh, M. & Satake, K., 2013b. The 21 May 2003 tsunami in the Western Mediterranean Sea: statistical and wavelet analyses, *Pure appl. Geophys.,* **170**(9-10), 1449–1462.

Heidarzadeh, M. & Satake, K., 2014a. Excitation of basin-wide modes of the Pacific Ocean following the March 2011 Tohoku tsunami, *Pure appl. Geophys.,* **171**(12), 3405–3419.

Heidarzadeh, M. & Satake, K., 2014b. The El Salvador and Philippines tsunamis of August 2012: insights from sea level data analysis and numerical modeling, *Pure appl. Geophys.,* **171**(12), 3437–3455.

Heidarzadeh, M. & Satake, K., 2015. New insights into the source of the Makran tsunami of 27 November 1945 from tsunami waveforms and coastal deformation data, *Pure appl. Geophys.,* **172**(3), 621–640.

Heidarzadeh, M., Satake, K., Murotani, S., Gusman, A.R. & Watada, S., 2015. Deep-water characteristics of the trans-Pacific tsunami from the 1 April 2014 Mw 8.2 Iquique, Chile Earthquake, *Pure appl. Geophys.,* **172**(3-4), 719–730.

Hébert, H., Heinrich, P., Schindelé, F. & Piatanesi, A., 2001. Far-field simulation of tsunami propagation in the Pacific Ocean: impact on the Marquesas Islands (French Polynesia), *J. geophys. Res.,* **106**(C5), 9161–9177.

IOC, IHO & BODC, 2014. *Centenary Edition of the GEBCO Digital Atlas, published on CD-ROM on behalf of the Intergovernmental Oceanographic Commission and the International Hydrographic Organization as part of the General Bathymetric Chart of the Oceans,* British Oceanographic Data Centre, Liverpool, UK.

Løvholt, F., Kaiser, G., Glimsdal, S., Scheele, L., Harbitz, C.B. & Pedersen, G., 2012. Modeling propagation and inundation of the 11 March 2011 Tohoku tsunami, *Nat. Hazards Earth Syst. Sci.,* **12**(4), 1017–1028.

Mofjeld, H.O., 2009. Tsunami measurements, in *The Sea,* Vol. 15, pp. 201–235, eds Robinson, A. & Bernard, E., Harvard University Press.

Okada, M., 1995. Tsunami observation by ocean bottom pressure gauge, in *Tsunami: Progress in Prediction, Disaster Prevention and Warning,* pp. 287–303. Springer.

Okada, Y., 1985. Surface deformation due to shear and tensile faults in a half-space, *Bull. seism. Soc. Am.,* **75**, 1135–1154.

Okal, E.A., Reymond, D. & Hébert, H., 2014. From earthquake size to far-field tsunami amplitude: development of a simple formula and application to DART buoy data, *Geophys. J. Int.,* **196**(1), 340–356.

Rabinovich, A.B., 1997. Spectral analysis of tsunami waves: separation of source and topography effects, *J. geophys. Res.,* **102**(12), 663–676.

Rabinovich, A.B., Candella, R.N. & Thomson, R.E., 2013. The open ocean energy decay of three recent trans-Pacific tsunamis, *Geophys, Res. Lett.,* **40**(12), 3157–3162.

Rabinovich, A.B. & Eblé, M.C., 2015. Deep-ocean measurements of tsunami waves, *Pure appl. Geophys.,* **172**(12), 3281–3312.

Saito, T., Matsuzawa, T., Obara, K. & Baba, T., 2010. Dispersive tsunami of the 2010 Chile earthquake recorded by the high-sampling-rate ocean-bottom pressure gauges, *Geophys. Res. Lett.,* **37**(23), doi:10.1029/2010GL045290.

Satake, K., 1995. Linear and nonlinear computations of the 1992 Nicaragua earthquake tsunami, *Pure appl. Geophys.,* **144**, 455–470.

Satake, K., Fujii, Y., Harada, T. & Namegaya, Y., 2013. Time and space distribution of coseismic slip of the 2011 Tohoku earthquake as inferred from tsunami waveform data, *Bull. seism. Soc. Am.,* **103**(2B), 1473–1492.

Synolakis, C. & Bernard, E., 2006. Tsunami science before and beyond Boxing Day 2004, *Phil Trans R Soc A,* **364**, 2231–2265.

Takagawa, T., 2013. Dispersion analysis of tsunami propagation with the consideration of water compressibility and earth elasticity for the improvement of prediction accuracy of far-field tsunamis, *J. Japan Soc. Civil Eng., Ser. B2,* **69**(2), 426–430.

Torrence, C. & Compo, G., 1998. A practical guide to wavelet analysis, *Bulletin of the American Meteorological Society,* **79**, 61–78.

Watada, S., Kusumoto, S. & Satake, K., 2014. Traveltime delay and initial phase reversal of distant tsunamis coupled with the self-gravitating elastic Earth, *J. geophys. Res.,* **119**(5), 4287–4310.

Weatherall, P., Marks, K.M., Jakobsson, M., Schmitt, T., Tani, S., Arndt, J.E. & Wigley, R., 2015. A new digital bathymetric model of the world's oceans, *Earth Space Sci.,* **2**(8), 331–345.

Welch, P., 1967. The use of fast Fourier transform for the estimation of power spectra: A method based on time averaging over short, modified periodogram, *IEEE Transactions on Audio and Electroacoustics,* **AE-15**, 70–73.

Wessel, P. & Smith, W.H.F., 1998. New improved version of generic mapping tools released, *EOS, Trans. Am. geophys. Un.,* **79**(47), 579.

Zaytsev, O., Rabinovich, A.B. & Thomson, R.E., 2016. A comparative analysis of coastal and open-ocean records of the great Chilean tsunamis of 2010, 2014 and 2015 off the coast of Mexico, *Pure appl. Geophys.,* **173**(12), 4139–4178.

Zaytsev, O., Rabinovich, A.B. & Thomson, R.E., 2017. The 2011 Tohoku tsunami on the coast of Mexico: A case study, *Pure appl. Geophys.,* **174**(8), 2961–2986.